MDPI

Communication

The Effect of IMCs and Segregation on the Microstructure and Mechanical Properties of β-Type Titanium Alloys

Xi-Long Ma [1],*, Bo-Wen Jia [1], Guo-Quan Nie [2], Zhi-Feng Shang [1], Bin-Bin Fu [1] and He Ren [1]

1 School of Materials Science and Engineering, Shijiazhuang Tiedao University, Shijiazhuang 050043, China
2 School of Mechanical Engineering, Shijiazhuang Tiedao University, Shijiazhuang 050043, China
* Correspondence: maxilong@stdu.edu.cn

Abstract: Two new β-type titanium (β-Ti) alloys of Ti-10.5Cr-5.4Mn-2.4Zr-0.9Al and Ti-15.6Cr-12Mn-3.3Zr were designed with the same bond order value 2.79 and different d-orbital energy level values of 2.28 and 2.16, respectively. The effect of intermetallic compounds (IMCs) and the segregation behaviors of β-Ti alloys were discussed by adding excessive and normal alloying elements to alloys under both as-cast and solution-treated conditions. The mono-β phase in the Ti-10.5Cr-5.4Mn-2.4Zr-0.9Al alloy and β+intermetallic compounds (IMCs) in the Ti-15.6Cr-12Mn-3.3Zr alloy were identified and observed. The as-cast and solution-treated alloys showed their ultimate tensile strength and fracture strain; these were 982 and 1002 MPa, with 9.82 and 9.89% for Ti-10.5Cr-5.4Mn-2.4Zr-0.9Al, and 448 and 296 MPa, with 0.12 and 0.11% for Ti-15.6Cr-12Mn-3.3Zr, respectively. Moreover, the Vickers hardness values of the as-cast and solution-treated alloys were 345 and 355 for Ti-10.5Cr-5.4Mn-2.4Zr-0.9Al, and 422 and 466 for Ti-15.6Cr-12Mn-3.3Zr, respectively.

Keywords: β-type titanium alloys; segregation behaviors; microstructure and mechanical properties; cold crucible levitation melting

1. Introductions

β-type titanium (β-Ti), possessing a unique corrosion resistance, biocompatibility, shape memory effect and high specific strength, has been extensively used in industrial, implant and aerospace applications [1–5]. However, the cost of β-Ti alloys is relatively higher than many other structural alloys due to the expensive raw materials and complex post-treatment processes, which limits their further application, such as in civilian and high-friction working fields [6,7]. Some approaches were carried out by researchers to reduce the cost of β-Ti alloys, such as the development of β-Ti alloys with cheap alloying elements and the proposal of β-Ti alloys with simplified post-treatment procedures [8,9]. Solid solution strengthening is also a possible approach to improve the mechanical properties of β-Ti alloys by adding a high content of alloying elements [10,11]. The super-plasticity performance and tensile properties of Ti alloys were enhanced by optimizing their compositions with Ni and Co alloying elements [12]. The compressive fracture strength and yield strength were improved with a high content of the Fe alloying element [13]. A high impressive tensile plasticity was achieved by the addition of Nb, Co, Cu and Al [14,15]. The effect of Cr content on the structure and mechanical properties of β-Ti alloys showed fine and large deformation dimples corresponding to the satisfied ductile fracture [16,17]. A reduction in costs was achieved by choosing Mn as a β stabilizer alloying element for biomedical applications [18]. The hydrogen storage capacities and hydrogen desorption plateau pressure behaviors were optimized by adjusting the contents of Cr and Mn in Ti alloys [19]. The addition of alloying elements greatly improved the mechanical properties of Ti alloys.

However, intermetallic compounds (IMCs) occur with the increase in additional elements, and the presence of IMCs in Ti alloys could lead to varying mechanical properties.

The service temperature range and high-temperature oxidation resistance ability were raised by the development of Ti-Al intermetallic compounds and the addition of tungsten [20–22]. IMCs might improve or decrease the mechanical properties of Ti alloys, depending on the content and types of alloying elements [23]. The improvement in Vickers hardness was demonstrated in Ti-Cr binary alloys when the Cr content was 80% in the $TiCr_2$ phase [24]. The addition of a suitable carbon content to TiAl alloys improved their flexural strength [25]. The precipitation of Heusler-type IMCs in materials strengthened their properties at elevated temperatures [26]. In particular, the negative effects of IMCs on alloys also occurred with a high content of additional elements or generation behaviors, such as the severe attenuation of ductility or uncontrollable mechanical properties [25,26]. Therefore, the discussion and identification of the influence of IMCs and segregation behaviors in multi-component β-Ti alloys is important and meaningful. The occurrence of IMCs could be approximately predicted using the d-orbital energy level (Md_t) and the bond-order (Bo_t) parameters based on the positions of alloys in the Md_t-Bo_t diagram [10].

In the past, repeated experiments and some empirical rules were applied to develop β-Ti alloys, which were relatively high-cost and inefficient [27]. M. Morinaga et al. calculated the Md_t and Bo_t values of varied elements using the MTi14 cluster and MTi18 models, respectively [28]. High-temperature alpha-type alloys, high-strength beta-type alloys, and high-corrosion-resistance alloys have been developed by considering their Bo and Md values and positions in the Md_t-Bo_t diagram [29]. The adaptation of the d-electrons concept could be used to design new composition β-Ti alloys conveniently and effectively at a reduced cost [10,28,30]. The Md_t-Bo_t diagram was widely used to predict the chemical properties, deformation types and mechanical properties of β-Ti alloys [1,11]. The stability of the β phase with respect to the e/a ratio and Mo equivalent numbers is an effective way to predict the phase stability and mechanical properties of β-Ti alloys, including Zr, Mn and Cr alloying elements [1,31]. For the metastable β-Ti alloys developed for orthopedic applications, their electron-to-atom (e/a) ratio is about 4.24, which ensures that they have a lower elastic modulus to alleviate the "stress shielding" effect [32]. The method of melting Ti alloys was very important when controlling their properties. If molten Ti makes contact with oxygen, nitrogen or hydrogen in the gas environment, reactions would occur during the melting process. The application of cold crucible levitation melting (CCLM) with an upper electric coil for heating and a lower electric coil for levitation could prevent molten material from contacting the crucible and maintain a high level of vacuum during the melting process [30].

In the present study, the two new compositional β-Ti alloys, Ti-10.5Cr-5.4Mn-2.4Zr-0.9Al and Ti-15.6Cr-12Mn-3.3Zr, were proposed with the same Bo_t value of 2.79 and different Md_t values of 2.28 and 2.16, respectively. The influences of IMCs and segregation behavior on the β-Ti alloys' microstructure and mechanical properties were evaluated by adding normal alloying elements to the Ti-10.5Cr-5.4Mn-2.4Zr-0.9Al alloy with an Md_t value of 2.28 and excessive alloying elements in the Ti-15.6Cr-12Mn-3.3Zr alloy with an Md_t value of 2.16. The CCLM method using the same processing parameters was applied to prepare the ingots of the two β-Ti alloys. The presence of IMCs in the β-Ti alloy Ti-15.6Cr-12Mn-3.3Zr was clearly observed in both as-cast and solution-treated conditions. The results showed that IMCs had negative effects on the tensile properties and positive effects on the Vickers hardness for β-Ti alloys. The solution-treated specimens of the two β-Ti alloys showed a larger grain size but higher Vickers hardness values than the as-cast specimens, which were influenced by their different segregation levels.

2. Experiment

2.1. Design and Preparation of Alloys

The raw materials with Ti, Zr, Cr, Mn and Al purities of 99.8, 98.0, 99.9, 99.9 and 99.9 mass%, respectively, were used to produce the two β-Ti alloys. The two new compositional β-Ti alloys, Ti-10.5Cr-5.4Mn-2.4Zr-0.9Al and Ti-15.6Cr-12Mn-3.3Zr, were designed with the same Bo_t value of 2.79 and different Md_t values of 2.28 and 2.16, respectively. The

mean values of Bo_t and Md_t of the two β-Ti alloys were calculated on the basis of the MTi14 cluster model, using Equations (1) and (2) [27,29].

$$Bo_t = \sum X_i (Bo)_i \tag{1}$$

$$Md_t = \sum X_i (Md)_i \tag{2}$$

where X_i is the molar fraction of component i in the alloy and $(Md)_i$ and $(Bo)_i$ are the numerical values of Md_t and Bo_t for each component i, respectively [27]. The compositions of Ti-10.5Cr-5.4Mn-2.4Zr-0.9Al and Ti-15.6Cr-12Mn-3.3Zr alloys are given in mass%. The CCLM method with the same processing parameters was applied to prepare the ingots of the two β-Ti alloys. The capacity of copper crucibles for CCLM equipment was 1 kg Fe. The upper electric coils with a rated power of 100 kW and the lower electric coils with a rated power of 60 kW provided energy for the melting and levitation of alloys. The levitation of molten titanium alloys avoided direct contact with the copper crucible during the production process. The melting points of the two β-Ti alloys were approximately 2150 K; their melting process was kept at 2350 K for 300 s under an argon (Ar) atmosphere with a purity of 99.99%. Then, the electrical supply of both the upper and lower coils was gradually decreased until it was switched off. After 1800s, the ingots cooled and solidified in the copper crucible. The as-cast specimens of the two β-Ti alloys were processed from the rectangle blocks cut from the ingots. The heating temperature and holding time for the solution treatment were 1173 K and 3.6 ks, respectively. Specimens cut from ingots were sealed in a quartz tube with an Ar atmosphere and the quenching process was carried out using cold water.

2.2. Detection Method

The microstructures of the two β-Ti alloys were observed by Optical Microscopy (OM) analysis. Sandpaper ranging from 80 to 2500 mesh was applied to ground OM specimens, and polishing paper was used to polish OM specimens. Distilled water, nitric acid, and hydrofluoric acid with volume percentages of 95%, 3% and 2% were mixed for etching OM specimens. The X-ray diffraction (XRD) was carried out to identify the phases and lattice constants of the two β-Ti alloys. The Cu Kα radiation of XRD was generated at 40 kV and 30 mA at room temperature. The point analysis was applied to the measurement of the chemical compositions of the two β-Ti alloys using an electron probe micro-analyzer (EPMA). For tensile test specimens, the gauge sizes had a diameter of 6 mm and length of 20 mm, and the grip diameter was 10 mm. The initial strain rate for the tensile tests was 1.9×10^{-4} s^{-1} at ambient temperature. The stress–strain curves of specimens were measured by the tensile test machine, while the ultimate tensile strength (σ_{UTS}) and fracture strain (ε_f) of specimens were obtained by using an extensometer during the tensile test. The load and holding time for Vickers hardness were 300 N and 10 s, respectively.

3. Results

3.1. Microstructure

The OM images of the Ti-10.5Cr-5.4Mn-2.4Zr-0.9Al and Ti-15.6Cr-12Mn-3.3Zr alloys in as-cast and solution-treated conditions are shown in Figure 1. For the Ti-10.5Cr-5.4Mn-2.4Zr-0.9Al alloy shown in Figure 1a,b, the mono-β phase was observed both in as-cast and solution-treated specimens. However, the existence of dual-β and IMCs phases was observed in the Ti-15.6Cr-12Mn-3.3Zr alloy, as shown in Figure 1c,d. The segregation of alloying elements occurred at grain boundaries and towards the grain interior. The average grain sizes of the two alloys under both conditions were obtained by measuring their mean intercept length. The average grain sizes of the as-cast and solution-treated Ti-10.5Cr-5.4Mn-2.4Zr-0.9Al alloys were 235 and 242 μm, respectively. Moreover, the average grain sizes of the as-cast and solution-treated Ti-15.6Cr-12Mn-3.3Zr alloys were 175 and 185 μm, respectively. The refinement of the grain size of the β-Ti alloys was measured with the

decrease in the Md_t value, corresponding to the increasing content of the alloying elements. The higher content of the alloying elements provided more nucleation opportunities for the titanium alloys, resulting in reduced grain sizes [33,34]. The solution treatment caused a growth in grain size in the two β-Ti alloys. The area fractions of the β and IMCs phases of the two β-Ti alloys were calculated via imaging analysis on the basis of their respective OM images. The absence of IMCs was observed in both as-cast and solution-treated Ti-10.5Cr-5.4Mn-2.4Zr-0.9Al alloys. In contrast, the area fractions of IMCs in the as-cast and solution-treated Ti-15.6Cr-12Mn-3.3Zr alloys were 30.2% and 28.3%, respectively.
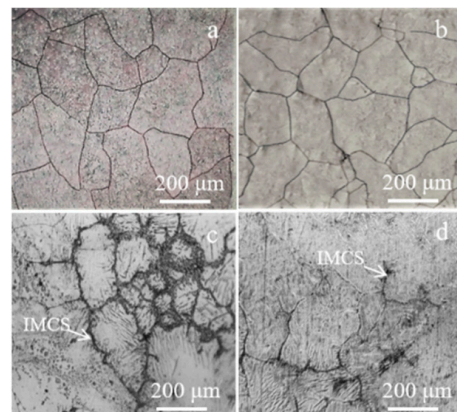
Figure 1. OM images of (**a**) and (**b**) Ti-10.5Cr-5.4Mn-2.4Zr-0.9Al and (**c**) and (**d**) Ti-15.6Cr-12Mn-3.3Zr alloys in as-cast and solution-treated conditions.

The XRD patterns of Ti-10.5Cr-5.4Mn-2.4Zr-0.9Al and Ti-15.6Cr-12Mn-3.3Zr alloys are shown in Figure 2. The mono-β phase was identified in both as-cast and solution-treated Ti-10.5Cr-5.4Mn-2.4Zr-0.9Al alloys, as revealed in Figure 2a,b. The $TiCr_2$ and TiCrMn IMCs in the Ti-15.6Cr-12Mn-3.3Zr alloy were detected via XRD, as shown in Figure 2c,d. Both $TiCr_2$ and TiCrMn were brittle phases; TiCrMn was formed by substituting Cr with Mn in the $TiCr_2$ lattice and the atomic stacking of TiCrMn was closer than previously detected in $TiCr_2$ [35]. The shift in the interatomic layer distances was primarily observed from (110) reflections. The respective lattice constants of the as-cast Ti-10.5Cr-5.4Mn-2.4Zr-0.9Al and Ti-15.6Cr-12Mn-3.3Zr alloys were 0.325 and 0.321 nm. The atomic radius of alloying elements Cr and Mn was smaller than Ti, while a decrease in the lattice constants of β-Ti alloys occurred with the increase in the alloying elements Cr and Mn. The phase compositions of the two β-Ti alloys detected via XRD agreed with the OM observation results.
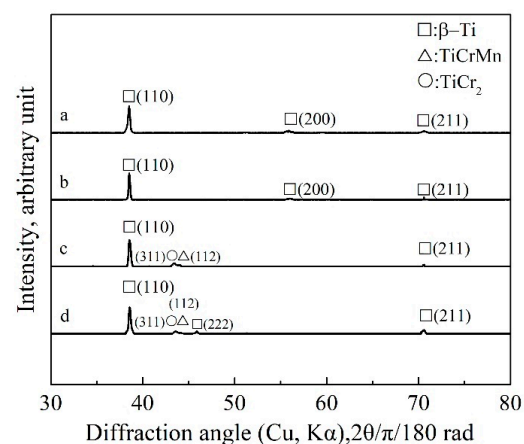
Figure 2. XRD patterns of (**a**) and (**b**) Ti-10.5Cr-5.4Mn-2.4Zr-0.9Al, (**c**) and (**d**) Ti-15.6Cr-12Mn-3.3Zr alloys in as-cast and solution-treated conditions, respectively.

3.2. Tensile Properties and Fracture Morphologies

The tensile curves of Ti-10.5Cr-5.4Mn-2.4Zr-0.9Al and Ti-15.6Cr-12Mn-3.3Zr alloys are shown in Figure 3a and b, respectively. The Ti-10.5Cr-5.4Mn-2.4Zr-0.9Al alloy with the mono-β phase showed slip deformation behavior, as revealed in Figure 3a. The Ti-15.6Cr-12Mn-3.3Zr alloy with β+IMCs phases fractured during the elastic stage, as shown in Figure 3b. The σ_{UTS} with ε_f values of the Ti-10.5Cr-5.4Mn-2.4Zr-0.9Al alloy in as-cast and solution-treated conditions were 982 MPa with 9.82% and 1002 MPa with 9.89%, respectively. The occurrence of the lower σ_{UTS} in the Ti-10.5Cr-5.4Mn-2.4Zr-0.9Al alloy in the as-cast condition compared to that in the solution-treated condition might be influenced by the different segregation degrees of the alloying elements. The σ_{UTS} with ε_f values of the Ti-15.6Cr-12Mn-3.3Zr alloy in as-cast and solution-treated conditions were 448 MPa with 0.12% and 296 MPa with 0.11%, respectively. Superior σ_{UTS} and ε_f of the Ti-10.5Cr-5.4Mn-2.4Zr-0.9Al alloy were measured compared to those of the Ti-15.6Cr-12Mn-3.3Zr alloy with β+IMCs phases. For the Ti-15.6Cr-12Mn-3.3Zr alloy, the presence of brittle IMCs near grain boundaries caused a severe deterioration in the tensile properties in both as-cast and solution-treated specimens.
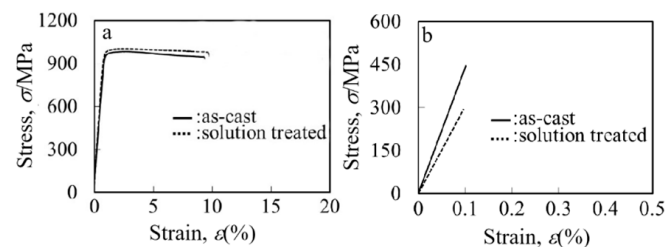
Figure 3. Tensile curves of (**a**) Ti-10.5Cr-5.4Mn-2.4Zr-0.9Al and (**b**) Ti-15.6Cr-12Mn-3.3Zr alloys in both as-cast and solution-treated conditions.

The fracture morphologies of Ti-10.5Cr-5.4Mn-2.4Zr-0.9Al and Ti-15.6Cr-12Mn-3.3Zr alloys in as-cast and solution-treated conditions are shown in Figure 4. The low- and high-magnification fracture morphologies of the as-cast Ti-10.5Cr-5.4Mn-2.4Zr-0.9Al alloy are shown in Figure 4a,b, and those of the solution-treated Ti-10.5Cr-5.4Mn-2.4Zr-0.9Al alloy are shown in Figure 4e and f, respectively. The dimple fracture patterns corresponding to the relative satisfaction ε_f values were observed in the Ti-10.5Cr-5.4Mn-2.4Zr-0.9Al alloy under both conditions. However, for the as-cast and solution-treated Ti-15.6Cr-12Mn-3.3Zr alloy, as shown in Figure 4c,g, brittle fracture inter- and trans-granular deformations occurred during the tensile test. The higher magnification of the vertical fractography of the Ti-15.6Cr-12Mn-3.3Zr alloy in as-cast and solution-treated conditions is shown in Figure 4d,h. The segregation of TiCrMn and $TiCr_2$ brittle IMCs at grain boundaries and interiors was clearly observed and resulted in the fracture of tensile specimens during the elastic deformation stage. The IMCs of TiCrMn and $TiCr_2$ provided the crack-propagation paths, which had negative effects on the tensile properties of the β-Ti alloys. Consistent results regarding IMC positions can also be observed in Figure 1.
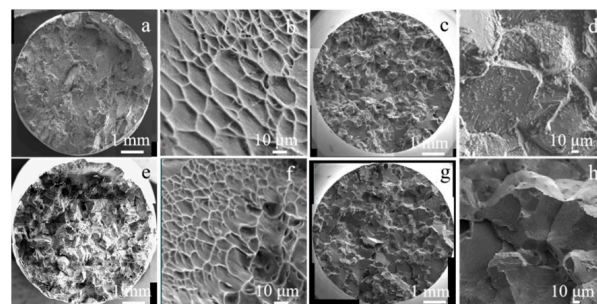
Figure 4. Fracture morphologies of (**a**,**b**,**e**,**f**) of Ti-10.5Cr-5.4Mn-2.4Zr-0.9Al and (**c**,**d**,**g**,**h**) of Ti-15.6Cr-12Mn-3.3Zr in as-cast and solution-treated conditions, respectively.

3.3. Point Analyses and Mappings

The compositional and SEM images of the cross-section and EPMA mappings of the Ti-15.6Cr-12Mn-3.3Zr alloy in the as-cast condition are shown in Figure 5. The compositional and SEM images of the cross-section of the fractured Ti-15.6Cr-12Mn-3.3Zr specimen indicated the locations of IMCs, as shown in Figure 5a,b. IMCs with higher luminosity were observed in the compositional image in Figure 5a, corresponding to the segregation of Cr and Mn elements with higher atomic quantity than Ti. At the same time, the similar phenomenon also occurred in the SEM image as shown in Figure 5b. The distributions of Ti, Zr, Cr and Mn elements in grains are revealed in Figure 5c–f. The relatively uniform distribution of the Ti and Zr element in alloys should be attributed to their similar atomic sizes and the continuous solid solution of Ti and Zr elements, as shown in Figure 5c,d. Higher Cr and Mn contents near grain boundaries compared to inner grains are observed in EPMA mappings, as shown in Figure 5e,f. The degree of segregation of alloying elements in the Ti-15.6Cr-12Mn-3.3Zr alloy was evaluated via point analysis. Detailed chemical compositions of the different positions in the Ti-15.6Cr-12Mn-3.3Zr alloy are listed in Table 1. The measuring positions of the point analysis are shown in Figure 5a ①–⑤. Point analysis of as-cast Ti-15.6Cr-12Mn-3.3Zr alloy, as shown in position ①, indicating the contents of Ti, Zr, Cr and Mn in the central part of the grain, respectively. The concentration heterogeneity of alloying elements and Ti was observed and measured at positions close to grain boundaries, as shown in positions ②, ③ and ④. The aggregation of Cr and Mn led to the formation of IMCs in grains during the solidification process. The segregation of Cr and Mn elements occurred at grain boundaries and showed a tendency to spread to inner grains. In addition, the distributions of Ti, Zr, Cr and Mn elements in position ① are the same with position ⑤. The distribution and concentration of alloying elements in as-cast Ti-11.0Cr-6.0Mn-4.4Zr-0.5Al and Ti-13.0Zr-6.0Cr-6.0Mn-5.0V grains were further clarified via point analyses, as shown in Figure 6a and b, respectively. Point analyses were performed 30–70 times to measure at least two grains of each alloy. Cr and Mn elements had a higher content around the grain boundaries compared to the center part of grains, which was consistent with the compositional, SEM and mapping results, as shown in Figure 5.
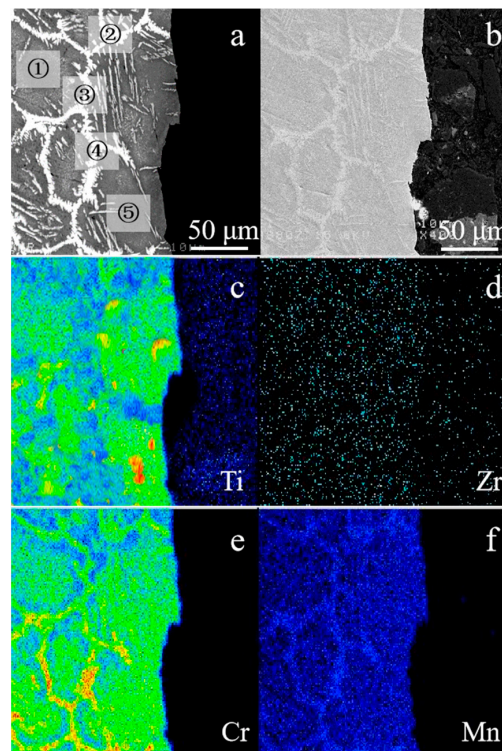
Figure 5. Compositional and SEM images of as-cast Ti-15.6Cr-12Mn-3.3Zr alloy, mapping analysis indicating the Ti, Zr, Cr and Mn distributions, respectively.

Table 1. Point analyses of as-cast Ti-15.6Cr-12Mn-3.3Zr alloy, indicating the contents of Ti, Zr, Cr and Mn, respectively.

Positions	Ti	Zr	Cr	Mn	Total (wt.%)
①	bal.	3.7	11.9	10.1	100.0
②	bal.	3.1	38.8	19.6	100.0
③	bal.	4.1	32.9	19.3	100.0
④	bal.	3.9	30.9	22.4	100.0
⑤	bal.	3.8	11.2	8.3	100.0
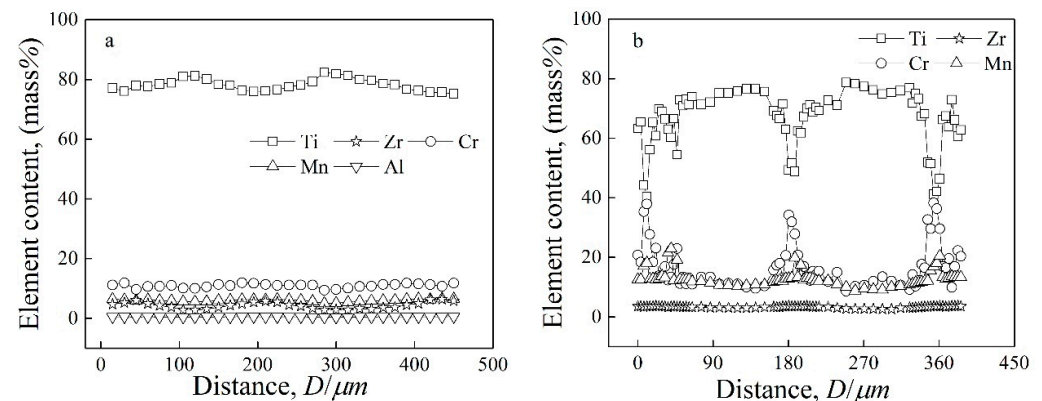
Figure 6. Concentration profiles of alloying elements of as-cast (**a**) Ti-10.5Cr-5.4Mn-2.4Zr-0.9Al and (**b**) Ti-15.6Cr-12Mn-3.3Zr alloys.

3.4. Vickers Hardness

The Vickers hardness measurements of the two β-Ti alloys are shown in Figure 7. The Vickers hardness values of the as-cast and solution-treated Ti-10.5Cr-5.4Mn-2.4Zr-0.9Al alloys were 345 and 355, respectively. Moreover, the Vickers hardness values of the as-cast and solution-treated Ti-15.6Cr-12Mn-3.3Zr alloys were 422 and 466, respectively. The two β-Ti alloys showed higher Vickers hardness values in solution-treated specimens than as-cast specimens, which should be attributed to the superior distribution of alloying elements. The refined grain size, solid solution strengthening of alloying elements and high hardness of TiCrMn and TiCr$_2$ IMCs improved the Vickers hardness values of the β-Ti alloys. Therefore, the Ti-15.6Cr-12Mn-3.3Zr alloy with an Md_t value of 2.16 showed higher Vickers hardness values compared with the Ti-10.5Cr-5.4Mn-2.4Zr-0.9Al alloy with an Md_t value of 2.28 in both as-cast and solution-treated conditions. In addition, the Vickers hardness of the two β-Ti alloys agreed with the tensile results, as shown in Figure 3.
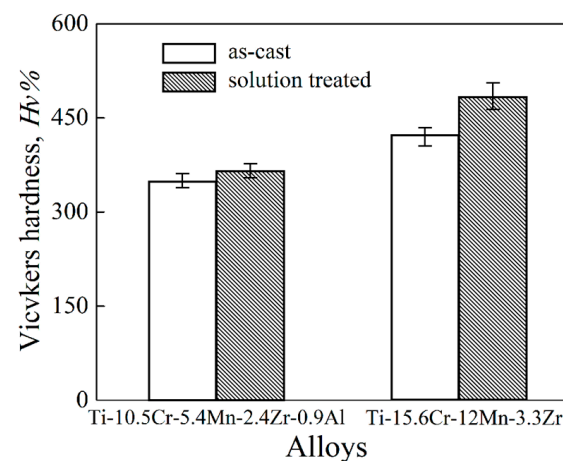
Figure 7. Vickers hardness of Ti-10.5Cr-5.4Mn-2.4Zr-0.9Al and Ti-15.6Cr-12Mn-3.3Zr alloys in as-cast and solution-treated conditions.

4. Conclusions

(1) Two new compositional β-Ti alloys of Ti-10.5Cr-5.4Mn-2.4Zr-0.9Al and Ti-15.6Cr-12Mn-3.3Zr were proposed with the same Bo_t value of 2.79 and different Md_t values of 2.28 and 2.16, respectively. The design of new compositional β-Ti alloys with high properties might be expected with a Bo_t value of 2.79 and Md_t value between 2.16 and 2.28.

(2) The mono-β phase was identified in both the as-cast and solution-treated Ti-10.5Cr-5.4Mn-2.4Zr-0.9Al alloys. Dual β+IMCs phases led to the severe deterioration in the tensile properties observed in the Ti-15.6Cr-12Mn-3.3Zr alloy. The brittle IMCs of TiCrMn and $TiCr_2$ provided crack propagation paths during the tensile process.

(3) The refined grain size, superior solid solution strengthening of the alloying elements and the presence of high-hardness TiCrMn and $TiCr_2$ IMCs improved the Vickers hardness values of the Ti-15.6Cr-12Mn-3.3Zr alloy compared to that of the Ti-10.5Cr-5.4Mn-2.4Zr-0.9Al alloy.

(4) In the two β-Ti alloys, the solution-treated specimens had a larger grain size but higher Vickers hardness values than the as-cast specimens, which could be attributed to the influence of their different segregation levels.

Author Contributions: Conceptualization, X.-L.M. and G.-Q.N.; methodology, X.-L.M. and Z.-F.S.; formal analysis, X.-L.M. and B.-W.J.; investigation, X.-L.M., B.-W.J., B.-B.F. and H.R.; writing—original draft preparation, X.-L.M.; writing—review and editing, X.-L.M., G.-Q.N. and Z.-F.S.; supervision, X.-L.M.; project administration, X.-L.M.; funding acquisition, X.-L.M., G.-Q.N. and Z.-F.S. All authors have read and agreed to the published version of the manuscript.

Data Availability Statement: Data will be provided upon request.

Conflicts of Interest: The authors declare no conflict of interest.

References

1. Sarabjeet, S.S.; Harpreet, S.; Mohamed, A.-H.G. A review on alloy design, biological response, and strengthening of β-titanium alloys as biomaterials. *Mater. Sci. Eng. C Mater. Biol. Appl.* **2021**, *121*, 111661. [CrossRef]
2. Juliana, D.C.T.; Claudemiro, B.; Andréa, C.D.R. Comparative analysis of corrosion resistance between beta titanium and Ti-6Al-4V alloys: A systematic review. *J. Trace Elem. Med. Biol.* **2020**, *62*, 12661. [CrossRef]
3. Yang, X.; Christopher, R.H. Corrosion-wear of β-Ti alloy TMZF (Ti-12Mo-6Zr-2Fe) in simulated body fluid. *Acta Biomater.* **2016**, *42*, 429–439. [CrossRef] [PubMed]
4. Gao, S.; Weng, F.; Bodunde, O.P.; Qin, M.; Liao, W.H.; Guo, P. Spatial characteristics of nickel-titanium shape memory alloy fabricated by continuous directed energy deposition. *J. Manuf. Process.* **2021**, *71*, 417–428. [CrossRef]
5. Yin, F.; Ma, S.; Hu, S.; Liu, Y.; Hua, L.; Cheng, G.J. Understanding the microstructure evolution and mechanical behavior of titanium alloy during electrically assisted plastic deformation process. *Mater. Sci. Eng. A* **2023**, *869*, 144815. [CrossRef]
6. Banerjee, D.; Williams, J.C. Perspectives on Titanium Science and Technology. *Acta Mater.* **2013**, *61*, 844–879. [CrossRef]
7. Hong, S.H.; Hwang, Y.J.; Park, S.W.; Park, C.H.; Yeom, J.T.; Park, J.M.; Kim, K.B. Low-cost beta titanium cast alloys with good tensile properties developed with addition of commercial material. *J. Alloys Compd.* **2019**, *793*, 271–276. [CrossRef]
8. Xu, Y.; Gao, J.; Huang, Y.; Rainforth, W.M. A low-cost metastable beta Ti alloy with high elastic admissible strain and enhanced ductility for orthopaedic application. *J. Alloys Compd.* **2020**, *835*, 155391. [CrossRef]
9. Li, M.; Geng, Y.; Liu, G.; Gao, Z.; Rui, X.; Xiao, S. Uncovering spatiotemporal evolution of titanium in China: A dynamic material flow analysis. *Resour. Conserv. Recycl.* **2022**, *180*, 106166. [CrossRef]
10. Ma, X.-L.; Matsugi, K.; Xu, Z.-F.; Choi, Y.-B.; Matsuzaki, R.; Lin, Z.-F.; Liu, X.-G.; Huang, H. Possibility of As-Cast Applications on β-Type Titanium Alloys Proposed in the Newly Expanded Area of *Bot-Mdt* Diagram. *Mater. Trans.* **2020**, *61*, 740–749. [CrossRef]
11. Jiang, X.J.; Zhou, Y.K.; Feng, Z.H.; Xia, C.Q.; Tan, C.L.; Liang, S.X.; Zhang, X.Y.; Ma, M.Z.; Liu, R.P. Influence of Zr content on β-phase stability in α-type Ti-Al alloys. *Mater. Sci. Eng. A* **2015**, *639*, 407–411. [CrossRef]
12. Anton, D.K.; Maria, N.P.; Ahmed, O.M.; Vladimir, V.C.; Anastasia, V.M. Microstructure and Superplastic Behavior of Ni-Modified Ti-Al-Mo-V Alloys. *Metals* **2022**, *12*, 741. [CrossRef]
13. Das, J.; Kim, K.B.; Baier, F.; Löser, W.; Gebert, A.; Eckert, J. Bulk ultra-fine eutectic structure in Ti–Fe–base alloys. *J. Alloys Compd.* **2007**, *28*, 434–435.

14. Okulov, I.V.; Bönisch, M.; Kühn, U.; Skrotzki, W.; Eckert, J. Significant tensile ductility and toughness in an ultrafine-structured Ti68. 8Nb13. 6Co6Cu5. 1Al6. 5 bi-modal alloy. *Mater. Sci. Eng. A* **2014**, *615*, 457. [CrossRef]

15. Kang, L.; Yang, C. A Review on High-Strength Titanium Alloys: Microstructure, Strengthening, and Properties. *Adv. Eng. Mater.* **2019**, *1801359*, 1–27. [CrossRef]

16. Lin, D.J.; Chern Lin, J.H.; Ju, C.P. Effect of chromium content on structure and mechanical properties of Ti-7.5 Mo-xCr alloys. *J. Mater. Sci. Mater. Med.* **2003**, *14*, 1–7. [CrossRef]

17. Hsu, H.C.; Wu, S.C.; Hsu, S.K.; Li, C.T.; Ho, W.F. Effects of chromium addition on structure and mechanical properties of Ti–5Mo alloy. *Mater. Des.* **2015**, *65*, 700–706. [CrossRef]

18. Alshammari, Y.; Yang, F.; Bolzoni, L. Mechanical properties and microstructure of Ti-Mn alloys produced via powder metallurgy for biomedical applications. *J. Mech. Behav. Biomed. Mater.* **2019**, *91*, 391–397. [CrossRef]

19. Cao, Z.; Ouyang, L.; Wang, H.; Liu, J.; Sun, D.; Zhang, Q.; Zhu, M. Advanced high-pressure metal hydride fabricated via Ti-Cr-Mn alloys for hybrid tank. *Int. J. Hydrogen Energy* **2015**, *40*, 2717–2728. [CrossRef]

20. Ying, Y.; Yongfeng, L.; Chan, L.; Junpin, L. Microstructure and Mechanical Properties of TiAl Matrix Composites Reinforced by Carbides. *Metals* **2022**, *12*, 790. [CrossRef]

21. Yan, M.; Yang, F.; Zhang, H.; Zhang, C.; Zhang, H.; Chen, C.; Guo, Z. Multiple intermetallic compounds reinforced Ti-48Al alloy with simple composition and high strength. *Mater. Sci. Eng. A* **2022**, *858*, 144152. [CrossRef]

22. Mo, T.; Chen, J.; Chen, Z.; Liu, J.; Zhou, Z.; He, W.; Liu, Q. Effect of intermetallic compounds (IMCs) on the interfacial bonding strength and mechanical properties of pre-rolling diffusion ARBed Al/Ti laminated composites. *Mater. Charact.* **2020**, *170*, 110731. [CrossRef]

23. Syed, F.J.; Chirag, D.R.; Muhammad, A.K.; Saad, J.K. Effect of Alloying Elements on the Compressive Mechanical Properties of Biomedical Titanium Alloys: A Systematic Review. *ACS Omega* **2022**, *34*, 29526–29542. [CrossRef]

24. Chen, K.C.; Allen, S.M.; Livingston, J.D. Microstructures of two-phase Ti–Cr alloys containing the TiCr$_2$ Laves phase intermetallic. *J. Mater. Res.* **1997**, *12*, 1472–1480. [CrossRef]

25. Bae, D.S.; Jang, S.J.; Yukawa, H.; Murata, Y.; Morinaga, M. Electronic States Calculation of Cobalt by Using the DV-Xα Cluster Method. *Mater. Trans.* **2001**, *42*, 1112–1118. [CrossRef]

26. Godor, F.; Palm, M.; Liebscher, C.H.; Stein, F.; Turk, C.; Leitner, K.; Rashkova, B.; Clemens, H. Microstructure Evolution of a New Precipitation-Strengthened Fe-Al-Ni-Ti Alloy down to Atomic Scale. *Metals* **2022**, *12*, 906. [CrossRef]

27. Masahiko, M. Alloy Design Based on Molecular Orbital Method. *Mater. Trans.* **2016**, *57*, 213–226. [CrossRef]

28. Morinaga, M.; Saito, J.; Morishita, M. Design of titanium alloys by means of a d-electrrons theory. *Light Met.* **1992**, *42*, 614–621. [CrossRef]

29. Masao, M.; Masahiro, C.; Yoshio, A.; Masahiko, M.; Natsuo, Y.; Hirohiko, A. Electronic States of the Cathodes of Titanium-based Alloys in Aqueous Corrosion. *Mater. Trans.* **1991**, *32*, 264–271. [CrossRef]

30. Ma, X.-L.; Matsugi, K.; Xu, Z.-F.; Choi, Y.-B.; Matsuzaki, R.; Hu, J.; Liu, X.-G.; Huang, H. Applicability of As-Cast on β Type Titanium Alloys Proposed in the Compositional Region with Different Tensile Deformation Types. *Mater. Trans.* **2019**, *60*, 2426–2434. [CrossRef]

31. Wang, Q.; Dong, C.; Liaw, P.K. Structural Stabilities of β-Ti Alloys Studied Using a New Mo Equivalent Derived from [β/(α+β)] PhaseBoundary Slopes. *Metall. Mater. Trans. A* **2015**, *46A*, 3441. [CrossRef]

32. Xiao, X.; Yang, K.; Lei, S.; Zhang, D.; Guo, L.; Dai, Y.; Lin, J. A β-type titanium alloy with high strength and low elastic modulus achieved by spinodal decomposition. *J. Alloys Compd.* **2023**, *963*, 171270. [CrossRef]

33. Murty, B.S.; Kori, S.A.; Chakraborty, M. Grain refinement of aluminium and its alloys by heterogeneous nucleation and alloying. *Int. Mater. Rev.* **2002**, *47*, 3–29. [CrossRef]

34. Kazuhiro, M.; Kiyoshi, S.; Yong, B.C.; Gen, S. Alloy Design of Ti Alloys Using Ubiquitous Alloying Elements and Characteristics of Their Levitation-Melted Alloys. *J. Jpn. Inst. Light Met.* **2012**, *62*, 486–492. [CrossRef]

35. Nong, Z.S.; Zhu, J.C.; Yang, X.W.; Cao, Y.; Lai, Z.H.; Liu, Y.; Sun, W. First-principles calculations of the stability and hydrogen storage behavior of C14 Laves phase compound TiCrMn. *Solid State Sci.* **2014**, *32*, 1–7. [CrossRef]